

Triggering of seismicity at short timescales following Californian earthquakes

D. Marsan

Laboratoire de Géophysique Interne et Tectonophysique, Université de Savoie, Le Bourget du Lac, France

Received 26 April 2002; revised 15 January 2003; accepted 11 February 2003; published 22 May 2003.

[1] A method for measuring seismicity rate changes caused by the occurrence of major earthquakes in the surrounding crust is proposed. It is based on a nonstationary Poisson modeling of earthquake activity. An estimate of the seismicity rate change and a probability measure of seismicity triggering following a large shock are derived, and the removal of the influence of independent aftershock sequences of other nearby, previous earthquakes is attempted, without using more traditional declustering techniques. The seismicity rate change estimator is corrected for its natural bias in favor of positive changes, at short timescales, that has so far strongly hindered measures of seismicity quiescences. Three Californian earthquakes are examined using this method: the 1989 $M7.1$ Loma Prieta, the 1992 $M7.3$ Landers, and the 1994 $M6.7$ Northridge earthquakes. Positive triggering is very commonly observed, as expected, but quiescence is, however, more seldomly obtained, for timescales up to 100 days after the main shock. This relative absence of quiescence, as compared to typical predictions of Coulomb modeling, for example, is also independently observed through direct correlation analyses of Californian seismicity. The possibility that the stresses caused by the main shock are spatially highly variable may explain these observations.

INDEX TERMS: 7209 Seismology: Earthquake dynamics and mechanics; 7223 Seismology: Seismic hazard assessment and prediction; 8123 Tectonophysics: Dynamics, seismotectonics; *KEYWORDS:* earthquake triggering, quiescence, fault interaction, seismicity

Citation: Marsan, D., Triggering of seismicity at short timescales following Californian earthquakes, *J. Geophys. Res.*, 108(B5), 2266, doi:10.1029/2002JB001946, 2003.

1. Introduction

[2] Triggering and modulations of seismicity activity by earthquakes are an ubiquitous phenomenon: aftershock sequences and clustered series of large magnitude events are common observations. How such changes in seismicity depend on both the relative locations of the faults and the time between the earthquake occurrences is still a widely open question. Spatial distribution of triggered activity strongly depends on the local fault network geometry, the slip distribution of the triggering shock, and more generally on the variability in the mechanical properties of the crustal volume surrounding the causative fault. Knowledge of the recent seismic history of the region is of great help in constraining this variability by imaging the locally active faults but can also be misleading as was for example illustrated by the 1994 Northridge earthquake which occurred on a concealed fault that was not recognized until the event struck [*Scientists of the U.S. Geological Survey and the Southern California Earthquake Center, 1994*].

[3] Nonetheless, the difficulty in predicting or modeling the spatial distribution of triggered sequences is not quite as great as our recurrent inability in understanding their temporal structure. Delays between apparently triggering

events and their offsprings can extend from seconds to tens of years, as is the case of long aftershock production. Temporal correlations between large earthquakes also develop over wide timescales [e.g., *Kagan and Jackson, 1991*]. Quite generally, an earthquake accommodates some of the local elastic strain, but also loads on-fault patches, neighboring and remote faults, that will in turn fail eventually. Relaxation of the tectonic strain is therefore a structured, complex phenomenon that involves large sets of earthquakes of different sizes, over spatial scales and timescales that can be much larger than the rupture length and duration of the initial, triggering earthquake.

[4] Ideally, one would like to estimate what are the changes in earthquake production that have been caused by a given earthquake (hereinafter referred to as main shock), and how those changes vary in space and time. The difficulty is here to make sure whether a given modulation in seismicity is effectively due to the main shock or not: while this can sometimes be trivial, as in the case of short timescales (i.e., with clear activity increases related to aftershock production), the problem becomes much more difficult at longer timescales. It corresponds to estimating the probability that a given earthquake would not have happened had the earlier main shock not occurred either. Computation of such a probability of triggering over various space and timescales should help our understanding of how earthquakes interact with each other, particularly in relation to

the predicted seismic response of a given crustal volume subject to stress changes, as given by friction models.

[5] In the past few years, several attempts have been made at determining, i.e., mapping, the spatial distribution of triggered activity following historical earthquakes [Reasenbergs and Simpson, 1992; Toda *et al.*, 1998; Stein, 1999; Wyss and Wiemer, 2000; Kilb *et al.*, 2000; Gombert *et al.*, 2001]. Regions of increased or decreased activity have thus been observed, and sometimes correlated to Coulomb triggering models (see Harris [1998] for a review on Coulomb modeling). However, such attempts generally suffer from one or several drawbacks, in particular:

[6] 1. Changes are calculated over arbitrary time periods, generally months to years before/after the main shock. The underlying assumption could be that such changes, or at least their spatial distribution, are more or less stationary over long (seconds/minutes to months/years) time periods. Such a hypothesis needs to be tested, especially as triggered events occurring within the chosen time period can play a significant role in locally modulating future activity (e.g., the 1999 Hector Mine, California, earthquake being triggered by aftershocks of the Landers earthquake as proposed by Felzer *et al.* [2003]; more generally, see also “epidemic type aftershock sequence” (ETAS), or branching models, for which cascading generation of earthquakes are modeled and analyzed [cf. Ogata, 1988]). Substantial alteration of the stress changes with time after the main shock, e.g., through further aftershock occurrences, should therefore lead to related changes in terms of seismicity triggering.

[7] 2. Spurious effects due to large earthquakes that occurred before the main shock are sometimes overlooked, or even totally ignored. Observed changes in seismicity rates can be artificially shifted toward one direction (mostly toward activity decreases).

[8] 3. Measures of the seismicity activity changes are not always appropriate; their significance is generally not computed, or it is done by assuming Gaussianity of the activity time series, even though they are clearly not Gaussian (large departures from the mean, well above the standard deviation, are common observations for such time series, and cannot be explained by Gaussian distributions). This problem is particularly severe when one wants to measure seismicity rate changes at small spatial scales, e.g., in order to obtain detailed rate change maps, or for regions that were weakly active before the main shock. Poisson rather than Gaussian statistics then need to be considered.

[9] 4. Usual measures of seismicity rate changes (Z , β statistics, ratio of seismicity rates) are not equally sensitive to increases and decreases of seismicity. Quiescences are difficult to observe, especially in weakly active regions and at short timescales, since one needs to wait several typical return times to correctly estimate the change. This can explain why so-called stress shadows are obvious for great earthquakes (e.g., following the 1857 Fort Tejon and the 1906 San Francisco earthquakes [see Ellsworth *et al.*, 1981; Harris and Simpson, 1996, 1998; Jaumé and Sykes, 1996; Stein, 1999]) and for creeping segments that generally experience high rates of small earthquakes [Reasenbergs and Simpson, 1992; Lienkaemper *et al.*, 1997], but not so much in other cases.

[10] As an illustration to the first two points, Figure 1 show how previously reported activity decreases [Stein,

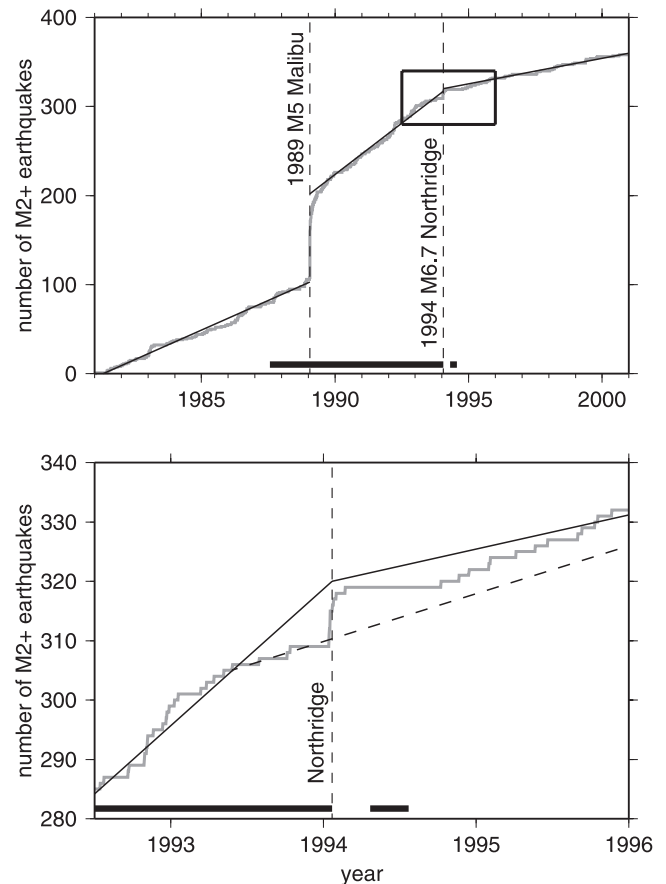


Figure 1. Cumulative number of $M2+$ earthquakes (SCSN catalogue) occurring (top) between 1981 and 2001 and (bottom) between 1992.5 and 1996 in a $25 \times 22 \text{ km}^2$ area (latitude between 33.85° and 34.05° , longitude between -118.8° and -118.5°) about 40 km south of Northridge epicenter. This area has been found by Stein [1999, Figure 2] to experience a decrease of activity following the 1994 Northridge earthquake. Thick horizontal bars indicate time intervals used by Stein [1999] in order to compute the seismicity rate change. Linear fits (black lines) are computed at large (~ 5 years) scale. Figure 1 (bottom) shows a close-up at shorter timescales, along with a better linear fit (dashed line) for this time interval.

1999] can be ambiguous. In this example, the Northridge earthquake is seen to trigger aftershocks in the analyzed region (a $\simeq 500 \text{ km}^2$ area about 40 km south of Northridge epicenter), this activation taking place in a rather silent interval that started several months prior to Northridge. The interpretation is made difficult by the fact that transient activity modulation activated by the 1989 $M5$ Malibu earthquake was still ongoing at the time of the Northridge earthquake. The graph shows a clear decrease of activity following Northridge, albeit a smaller one than the one reported by Stein [1999] for which the aftershock sequence of the 1989 Malibu earthquake was not accounted for. The mean rate does not recover its pre-Malibu state more than 6 years after Northridge. The close-up at shorter timescales (1992.5 to 1996) shows that large-scale observation is partly misleading: a better linear fit along with a burst of activity

just prior to Northridge indicates that the quiescence observed after 1994 is perhaps uncorrelated with Northridge as its origin can be tracked back several months before Northridge (also see *Dieterich and Okubo* [1996] for a similar observation and tentative interpretation in the case of Hawaiian seismicity), the latter main shock actually triggering seismicity in the region at the very short (i.e., days) timescale.

[11] This paper aims at examining these issues, by proposing a method for calculating less ambiguous, fine-scale maps of seismicity rate changes. It is structured as follows: the methodology is detailed in section 2. A model for investigating triggering/inhibition effects is described. A methodology is developed for taking previous aftershock sequences and preseismicity clusters into account, without resorting to traditional declustering methods that are not suited for this purpose. Appropriate Poissonian statistics are then proposed in order to measure rate changes, that are equally “fair” to both activation and deactivation. In section 3, the method is applied to three Californian earthquakes: the Loma Prieta, Northridge, and Landers earthquakes. The dependence of the triggered activity distribution with time is explored, for timescales up to 200 days. Longer timescales can prove to be difficult to analyze because of the difficulty of causally linking two events separated by several months/years. The main result of this study is that, contrary to previous observations and stress transfer modeling, activity decreases are too rarely observed for timescales up to 100 days. Direct correlation measures of Californian seismicity are given in section 4, and independently confirm this phenomenon. A possible scenario, based on rate-and-state friction combined with a strongly heterogeneous crust, is proposed in section 5 to explain these observations.

2. Estimating the Probability of Triggering and the Seismicity Rate Change: Method

[12] The problem of estimating seismicity rate changes can be summarized as follows. Consider a given crustal volume experiencing seismic activity, measured between $T_0 - t_B$ and $T_0 + t_A$, where T_0 is the occurrence time of the specific event (e.g., main shock) under study. It is assumed that no changes in detection level, magnitude scale, or monitoring coverage affects the volume.

[13] Activity occurring between $T_0 - t_B$ and T_0 (“pre-activity”) and between T_0 and $T_0 + t_A$ (“postactivity”) can be modeled as two Poisson random variables, with parameters $\lambda_B t_B$ and $\lambda_A t_A$; the rates λ_B and λ_A are the two unknowns. The difficulty lies in finding reliable probability distributions of their estimates $\hat{\lambda}_B$ and $\hat{\lambda}_A$. Then, knowing the probability density functions $f_B(\hat{\lambda}_B)$ and $f_A(\hat{\lambda}_A)$, it is straightforward to compute (1) a probability density $f(\hat{r})$ for the estimate of the seismicity rate change $\hat{r} = \hat{\lambda}_A/\hat{\lambda}_B$, which can be used to compute the mean log ratio $E\{\log \hat{r}\}$, and (2) the probability $\mathcal{P} = \Pr(\hat{\lambda}_A \geq \hat{\lambda}_B)$ that triggering has taken place. \mathcal{P} is constructed to measure how significant the seismicity rate change is, i.e., whether this change can be due to “pure luck” or to an actual change in the seismogenic process. $E\{\log \hat{r}\}$ estimates the mean log rate change, and differs from the logarithm of the sample ratio $r = n_A t_A / n_B t_B$ by fully accounting for natural variations in r also due to pure chance; this is especially important as we look at

short durations and small spatial scales, at which there is typically little seismicity. I detail in this section how to estimate these various quantities.

2.1. Poisson Process Modeling of Seismicity

[14] The number of earthquakes $n_{[t;t+\Delta t]}$ above a given threshold magnitude, occurring within a given time interval ($t; t + \Delta t$) and in a given volume ($\mathbf{r}; \mathbf{r} + \Delta \mathbf{r}$), can be modeled as a Poisson random variable of mean λ . The latter depends on both ($t; t + \Delta t$) and ($\mathbf{r}; \mathbf{r} + \Delta \mathbf{r}$), and is in effect the only parameter controlling n . More generally, earthquake activity in ($\mathbf{r}; \mathbf{r} + \Delta \mathbf{r}$) is an integer infinitely divisible random variable (regarding to both volume and time interval), and the Poisson distribution provides the simplest such random variable. One can therefore reduce the temporal evolution of $n_{[t;t+\Delta t]}$ to a nonstationary Poisson process, and thus to the evolution of $\lambda(t)$ such that

$$\Pr(n_{[t;t+\Delta t]} = n) = e^{-\lambda(t;t+\Delta t)} \frac{\lambda(t;t+\Delta t)^n}{n!} \quad (1)$$

$$\lambda(t;t+\Delta t) = \int_t^{t+\Delta t} ds \lambda(s) \quad (2)$$

where $\lambda(t)$ is the rate of earthquakes at time t in the considered volume, i.e., $\lambda(t) = \lim_{\Delta t \rightarrow 0} [\lambda(t;t+\Delta t)/\Delta t]$. Interaction models can be built on deriving the changes, over space and time, of λ . Various works have explored this type of modeling; see *Ogata* [1999] for a recent review on ETAS models, and see also the use of nonstationary Poissonian models for predicting seismic hazard related to aftershock sequences [*Reasenber and Jones*, 1989; *Wiemer*, 2000].

2.2. Stationary Model

[15] The simplest model assumes constant rates λ_B and λ_A over the two time intervals $[T_0 - t_B, T_0]$ and $[T_0, T_0 + t_A]$. The conditional density $f(\hat{\lambda}|n)$ that the n observed earthquakes are due to a Poisson random variable with mean $\hat{\lambda}t$ is simply $f(\hat{\lambda}|n) = \Pr(n|\hat{\lambda}t) = \exp(-\hat{\lambda}t) (\hat{\lambda}t)^n/n!$ since the a priori probability on λ is uniform. This yields that

$$f(\hat{\lambda}|n) = t e^{-\hat{\lambda}t} \frac{(\hat{\lambda}t)^n}{n!} \quad (3)$$

i.e., $f(\hat{\lambda}|n)$ is the gamma density $f_{t,n+1}$. As an example, let assume that $n_B = 28$ earthquakes occurred in the $t_B = 100$ days prior to T_0 , and that we observe $n_{A_1} = 3$, $n_{A_2} = 7$ and $n_{A_3} = 37$ earthquakes within $t_{A_1} = 10$, $t_{A_2} = 20$ and $t_{A_3} = 100$ days after T_0 , respectively. Figure 2 shows an example of such a process, along with the probability density functions associated to the estimates $\hat{\lambda}_B$, $\hat{\lambda}_{A_1}$, $\hat{\lambda}_{A_2}$ and $\hat{\lambda}_{A_3}$ as given by equation (3). As the time interval t_A of observation grows, more earthquakes are counted, and the pdf gets more and more peaked around the sample rate n_A/t_A . On the basis of those distributions, estimate of the distribution of the seismicity rate change \hat{r} and the probability of triggering \mathcal{P} can be obtained, as described in section 2.4. Note that the fact that $f(\hat{\lambda}|t)$ is a gamma density implies that the comparison, in the stationary case, of $\hat{\lambda}_A$ and $\hat{\lambda}_B$, as independent random

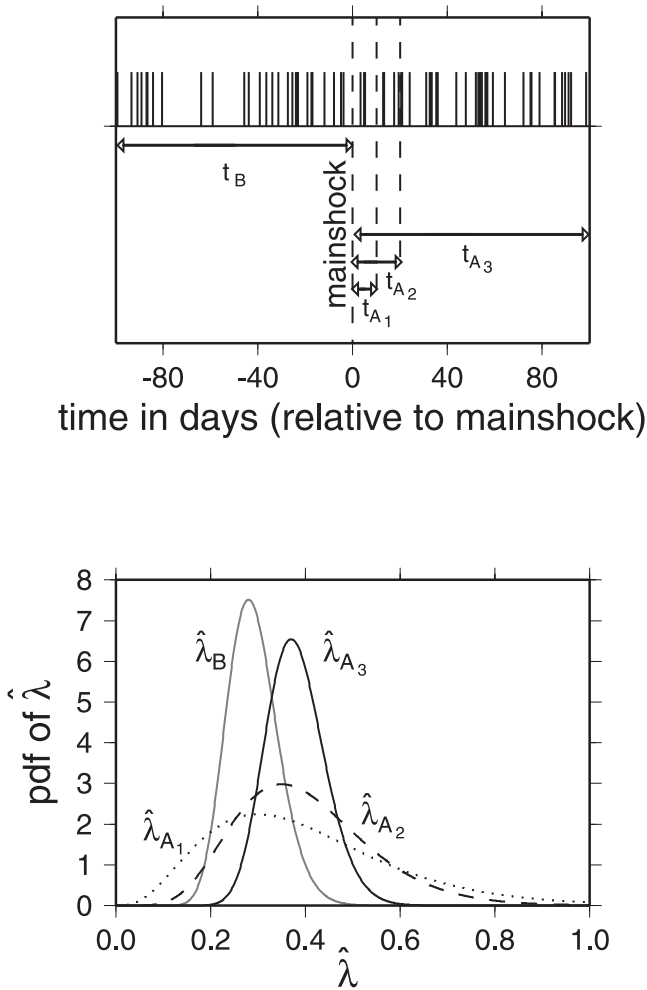


Figure 2. (top) Stationary model of seismicity with times of occurrence of synthetic earthquakes relative to the occurrence time of the main shock under study. (bottom) Probability density functions f of the seismicity rate $\hat{\lambda}_B$ (thin line), corresponding to $t < 0$, and the rates $\hat{\lambda}_{A_1}$ (dotted line), $\hat{\lambda}_{A_2}$ (dashed line) and $\hat{\lambda}_{A_3}$ (thick line) related to 10, 20 and 100 day intervals following the main shock. Narrowing of $f_A(\hat{\lambda}_A)$ at long durations is due to the gain of information on the process as more and more events are counted.

variables, is formally similar to the comparison of the sample variance of two independent distributions. As such, use of $E\{\log \hat{r}\}$ has a measure of the rate change is equivalent to using the mean of Fisher's Z statistic.

2.3. Nonstationary Model

[16] As explained in section 1, stationarity cannot generally be assumed, the less so at long (months/years) timescales. In particular, aftershock production decays with time after the occurrence of an earthquake. A common way to handle this issue is to decluster the catalogue; use of Reasenberg's [1985] method has, for example, been made by Kilb *et al.* [2000] and Wyss and Wiemer [2000]. Several critics can be formulated against such a type of procedure, at least for the present purpose of removing nonstationarity in the catalogue: (1) it is heavily dependent

on several parameters that are either largely arbitrary (P , Q of Reasenberg [1985]) or not always easy to confidently estimate (α , C , t_0 of Reasenberg [1985]); (2) it is not adaptive, though latter versions have considered updating the parameters as more data are obtained [e.g., Reasenberg and Jones, 1989]; (3) the underlying physics is questionable, in particular with regard to the boolean “ B is an aftershock/ B is not an aftershock of A ” representation, and also to the choice that a cluster “propagates” only through its largest and its latest members; and (4) it is not appropriate to the present problem. Declustering techniques are operational methods designed to roughly remove what common sense sees as aftershock sequences. The present problem involves keeping the triggered seismicity clustered after T_0 as it is its spatial and temporal distribution that is of interest. Overlapping of an ongoing past aftershock sequence with the one starting at T_0 , resulting in the merging of the two clusters, would have to be avoided. Finally, Wyss and Wiemer [2000] commented that their “results (did) not depend on the inclusion or exclusion of clusters” singled out by this declustering technique. This is a rather surprising statement, as the aftershock sequences of several earthquakes (and most particularly of the Joshua Tree earthquake) significantly perturb the estimate of the seismicity rate change, in the same way as shown in Figure 1 in the case of the Malibu and Northridge earthquakes.

[17] An interesting alternative to traditional declustering has recently been proposed by Zhuang *et al.* [2002]. A thinning procedure based on the probability that a given earthquake is triggered by a stationary background process rather than by a preceding earthquake is computed, exploiting the ETAS model. Use of a temporal ETAS models will be evoked later.

[18] The approach taken here is the following. Given some parameterized model of nonstationary seismicity, (1) the optimal set of parameters is computed by fitting the model to the data, (2) estimate of the distribution of seismicity rate $\hat{\lambda}_B$ that would be expected between T_0 and $T_0 + t_A$ if nothing special happens at T_0 is then derived, and (3) is compared to $f_A(\hat{\lambda}_A)$ obtained from equation (3). The algorithm then takes the following form:

[19] 1. The seismicity is spatially discretized in 2-D cells of size L .

[20] 2. Then, for each cell the discretized time series of activity $n(t)$ is computed, at a given temporal resolution Δt , between $T_0 - t_B$ and T_0 .

[21] 3. The best parameter set θ^* of a parameterized model λ_θ is searched for, by minimizing a cost function $J(\theta)$ defined from the Poissonian log likelihood function $J(\theta) = \sum_i \lambda_\theta(i) - n(i) \log \lambda_\theta(i)$. Note that in the continuous limit $\Delta t \rightarrow 0$, this yields the log likelihood function of Ogata [1988].

[22] 4. Extrapolation of λ_{θ^*} to $T_0 \leq t \leq T_0 + t_A$ is performed. The probability density of $\hat{\lambda}_B$ is then obtained, by perturbing θ around θ^* according to the standard deviation $\Delta\theta$ of the error on the parameters.

[23] 5. The parameter $f_B(\hat{\lambda}_B)$ is then compared to $f_A(\hat{\lambda}_A)$, obtained from equation (3), and constrained by the observed number of earthquakes n_A that occurred in the cell between T_0 and $T_0 + t_A$. A probability of triggering \mathcal{P} and the mean $E\{\log \hat{r}\}$ of the logarithm of the ratio estimate $\hat{r} = \hat{\lambda}_A / \hat{\lambda}_B$ can finally be computed.

[24] Choice of the cell length L is not innocuous. For too small a L , most (if not all) cells will have at most one earthquake, and no meaningful prediction on the future state of the system can be made, outside the trivial stationary scenario of section 2.2. Search for the best model requires enough data; here $L = 10$ km was chosen, so to be larger than the typical uncertainty on earthquake location. Influence of L on the calculated seismicity rate change maps will be discussed in the case of the Northridge earthquake. Use of full space-time models will be considered in a future work as a way to remove this dependence on L .

[25] Several models λ_θ were considered and tested in this study. These more particularly included three linear models: (1) an AR(P) model, (2) the discretized and continuous temporal ETAS models, and (3) a sum of power law relaxation curves.

2.3.1. AR(P) Model

[26] The AR(P) model gives

$$\lambda(i)\Delta t = \beta_0 + \sum_{j=1}^P \beta_j n(i-j) \quad (4)$$

For $P = 0$, one recovers the sample mean $\sum n(i)/t_B$ as the best β_0^* ; the estimate of λ is then the sample rate commonly used in seismicity rate change estimation. For $P > 0$, this sample rate is corrected, the estimated rate increasing when the local activity level increases.

[27] This model is computationally efficient, and reproduces the correlation existing in the time series $n(i)$. Experimenting with this model shows that the intermittency, i.e., the existence of large peaks in the time series, corresponding to the activity immediately following the occurrence of large earthquakes, is not well accommodated. A variation of this model is obtained by imposing $\beta_0 = 0$, with the consequence that the fit is globally worse, but can become locally better during periods outside aftershock sequences, since the model provides a more fluctuating moving average. Dependence on P is very weak as long as $P \geq t_A/\Delta t$; this is due to the fact that the first coefficients are generally strongly dominant.

2.3.2. Discretized/Continuous Temporal ETAS Model

[28] The previous model can be modified to account for the magnitude m of the earthquakes in the time series $n(i)$. A discretized version of the ETAS model can then be obtained, by assuming a power law decay $\beta_j \sim j^{-p}$ of the coefficients. The model takes the form

$$\lambda(i)\Delta t = \beta_0 + A \sum_{j \geq 1} j^{-p} n^{[\alpha]}(i-j) \quad (5)$$

where the time series is now $n^{[\alpha]}(i) = \sum n_m(i) 10^{\alpha m}$, i.e., the sum over m of the number $n_m(i)^m$ of earthquakes of magnitude m occurring at time step i weighted by a factor $10^{\alpha m}$. The time series $n(i)$ used in the previous model then corresponds to $n(i) = n^{[0]}(i)$. The parameter set reduces to $\theta = \{\beta_0, A, p, \alpha\}$. Note that the cutoff time usually introduced in the power law t^{-p} decay is here ignored, since the resolution timescale Δt used throughout this work is much longer than typical values of this cutoff. Discretization of the model allows for a much quicker numerical treatment, especially for very active regions.

[29] The more computationally expensive continuous ETAS model is also tested. Seismicity rate is then modeled as

$$\lambda(t) = \lambda_0 + A \sum_{i/t_i} (t - t_i + c)^{-p} 10^{\alpha m_i} \quad (6)$$

where the sum is on all earthquakes (t_i, m_i) with occurrence times $t_i < t$.

2.3.3. Sum of Power Law Relaxations

[30] This model takes the form

$$\lambda(i)\Delta t = \sum_{j=1}^P A_j (i - t_j)^{-p_j} \quad (7)$$

i.e., a linear combination of P power law basis functions. Each function is parameterized by three parameters $\{A, t, p\}$. No “background” coefficient β_0 is here needed as a constant term can be accommodated by taking $p = 0$ and $t \leq 0$. Dependence on P is weak, provided that it is larger than the number of dominant aftershock sequences that occurred between $T_0 - t_B$ and T_0 . The best results using this model were obtained by considering the cumulative time series rather than the time series itself. Of the various models tested, this one gives the best trade-off between short computation times and goodness of fit.

[31] A rather illustrative example is given in Figure 3, in the case of a slightly larger area than the one analyzed in Figure 1 centered on the 1989 M_5 Malibu earthquake. Change in the seismicity rate is examined relative to the occurrence of the Northridge earthquake. Time is discretized at $\Delta t = 10$ days, and (following Stein [1999]) the rate λ_A characterizes the time period extending between 3 months and 6 months after Northridge. An AR($P = 20$) model, with and without β_0 , a sum of $P = 6$ power laws, and the continuous ETAS model are fitted against the data starting in 1981 (Figure 3, top). All models predict more earthquakes in the 3 to 6 months interval than the actual $n_A = 1$ number. Figure 3 (bottom) displays the corresponding probability density functions of $\hat{\lambda}_A$ and $\hat{\lambda}_B$. For simplicity, $\hat{\lambda}_A$ and $\hat{\lambda}_B$ here refers to numbers rather than rates, i.e., they equal the rate times 90 days. A burst of activity (8 earthquakes in 10 days) occurs prior to Northridge. This burst significantly perturbs the AR models. The mean number of earthquakes per 10 days in this cell, for the 13 years prior to Northridge, is 0.891, hence 8.019 earthquakes for a 90 day interval. Use of this sample rate, i.e., mimicking the estimate of Stein [1999], would yield a mean $E\{\log \hat{r}\}$ and a probability of triggering \mathcal{P} intermediate between the AR models and both the continuous ETAS and the sum of power law models.

2.4. Estimate of the Seismicity Rate Change \hat{r} and Probability of Triggering \mathcal{P}

[32] Given the probability density functions of the estimates $f_A(\hat{\lambda}_A)$ and $f_B(\hat{\lambda}_B)$, the pdf $f(\hat{r})$ of the estimate $\hat{r} = \hat{\lambda}_A/\hat{\lambda}_B$ can be computed as

$$f(\hat{r}) = \int_0^\infty d\hat{\lambda}_B \hat{\lambda}_B f_B(\hat{\lambda}_B) f_A(\hat{r}\hat{\lambda}_B) \quad (8)$$

Calculations show that $E\{\hat{r}\} = (1 + n_a)E\{(\hat{\lambda}_B t_A)^{-1}\}$; in the stationary case, for which $f_B(\hat{\lambda}_B)$ is obtained from equation

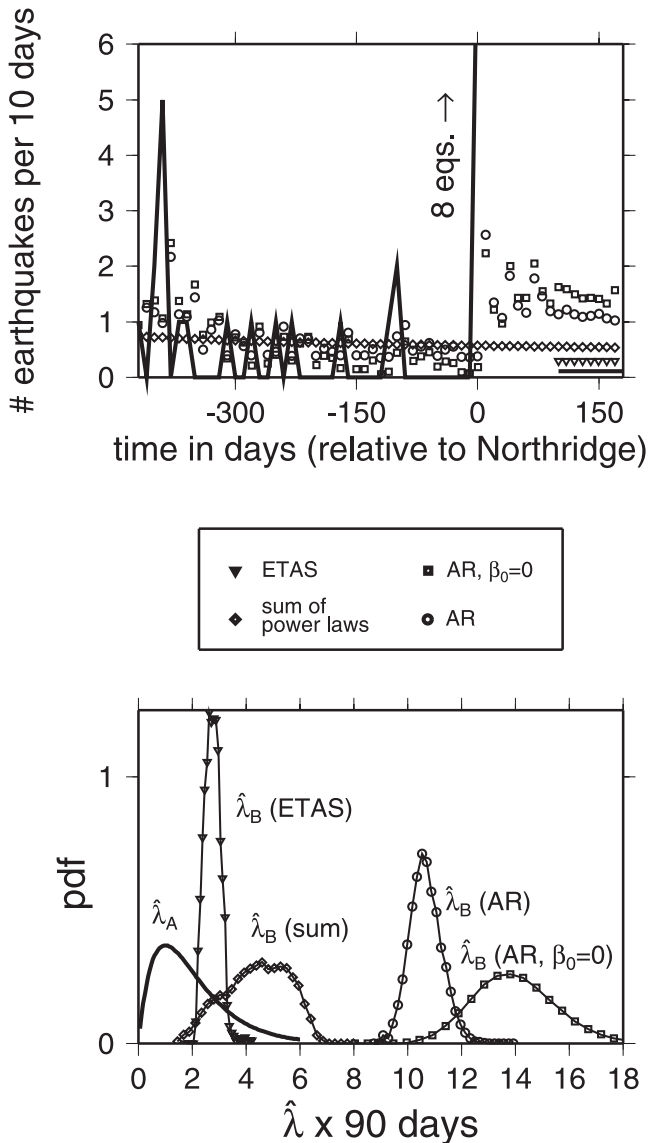


Figure 3. (top) Seismicity time series (thick line) around the 1989 $M5$ Malibu earthquake, in a $\approx 625 \text{ km}^2$ area, before and after the occurrence of the Northridge earthquake. Predictions for $90 < t_A < 180$ days, given by the AR, the continuous ETAS, and the sum of power law models, are shown. The discretization time step is $\Delta t = 10$ days. The mean number of earthquakes per 10 days occurring between 90 days and 180 days after Northridge is $1/9 = 0.11$ (thick segment, bottom right corner). The maximum likelihood rate (per 10 days) for the ETAS model is also shown (∇) for this interval. (bottom) Probability density functions of $\hat{\lambda}_A \times 90$ days and $\hat{\lambda}_B \times 90$ days, for the various models. These pdf are obtained by Monte Carlo perturbing the best parameter sets θ^* , with perturbations scaled by the standard deviation $\Delta\theta$ corresponding to the uncertainty on the best parameter set (inversion error).

(3), this mean is $E\{\hat{r}\} = [(1 + n_A)/n_B](t_B/t_A)$. The asymmetry between preparameters (B) and postparameters (A) makes this estimator a biased one. Instead, $E\{\log \hat{r}\} = E\{\log \hat{\lambda}_A\} - E\{\log \hat{\lambda}_B\}$ is used to characterize the rate change.

[33] The probability of triggering \mathcal{P} is defined as the probability that $\lambda_A > \lambda_B$, i.e.,

$$\mathcal{P} = \int_0^\infty d\hat{\lambda}_B f_B(\hat{\lambda}_B) \int_{\hat{\lambda}_B}^\infty d\hat{\lambda}_A f_A(\hat{\lambda}_A) \quad (9)$$

It corresponds to the probability that the estimated seismicity process is more active after the main shock than before. Given that $f_A(\hat{\lambda}_A)$ follows equation (3), it comes that $\mathcal{P} = 1 - E\{P(n_A + 1, \hat{\lambda}_B t_A)\}$ where P is the incomplete Gamma function. This probability is estimated numerically. Computation of $E\{\log \hat{r}\}$ and \mathcal{P} in the case of Figure 3 gives that $E\{\log \hat{r}\} = -0.957, -1.072, -0.353, -0.554$, and $\mathcal{P} = 0, 0, 0.227$ and 0.084 for the AR, the AR with $\beta_0 = 0$, the continuous ETAS, and the sum of power law models, respectively. Such values correspond to a case of quiescence. This quiescence is however not observed at shorter time intervals. Similar calculations, based on the sum of power law model, yield $E\{\log \hat{r}\} = 0.176$ and 0.165 for the first and the first two months after Northridge, respectively, and only indicate a quiescence when considering the first three months ($E\{\log \hat{r}\} = -0.139$).

2.5. Detectability of Quiescence Phenomena

[34] Detection of quiescence/activation phenomena can become a problem when looking at weakly active regions and short timescales. For example, when looking at a weakly active region that becomes even less active than it was before the main shock, the estimator $E\{\log \hat{r}\}$ can be shown to be biased in favor of positive triggering, i.e., it can give positive values when a negative one is expected. This bias is documented in Appendix A, and a practical correction is proposed in order to unbiased the estimator. Applying this correction to, e.g., $E\{\log \hat{r}\} = -0.353$ found for the continuous ETAS model of Figure 3 yield an estimated $E\{\log \hat{r}\} = -0.405$. \mathcal{P} is also biased; for example, taking $\lambda_A = \lambda_B$, \mathcal{P} is found to be larger than 0.5 for $t_A < t_B$, and smaller than 0.5 for $t_A > t_B$. However, this estimator can be used with $t_A = t_B$ and is then unbiased for detecting triggering/quiescence.

3. Triggering Following the Loma Prieta, the Landers, and the Northridge Earthquakes

[35] The method is now applied to three California earthquakes: the 1989 $M7.1$ Loma Prieta, the 1992 $M7.3$ Landers, and the 1994 $M6.7$ Northridge earthquakes. For each event, a region is selected, with a size a few times larger than the main shock rupture length. Earthquakes of magnitude larger than a magnitude threshold M_c were counted, and discretized on a grid with resolution length L : cells are separated by a distance L , but overlap as all the events occurring within a radius L of the cell center are counted for this cell. This results in all earthquakes to be counted for several cells. $L = 10 \text{ km}$ was chosen, so that it is larger than typical location errors; this value allows for a compromise between detailed enough triggering maps and active enough cells. Maps with $L = 5$ and 20 km were also computed for Northridge. For each cell, a number of “after events” n_A occurring within a time t_A following the main shock is then

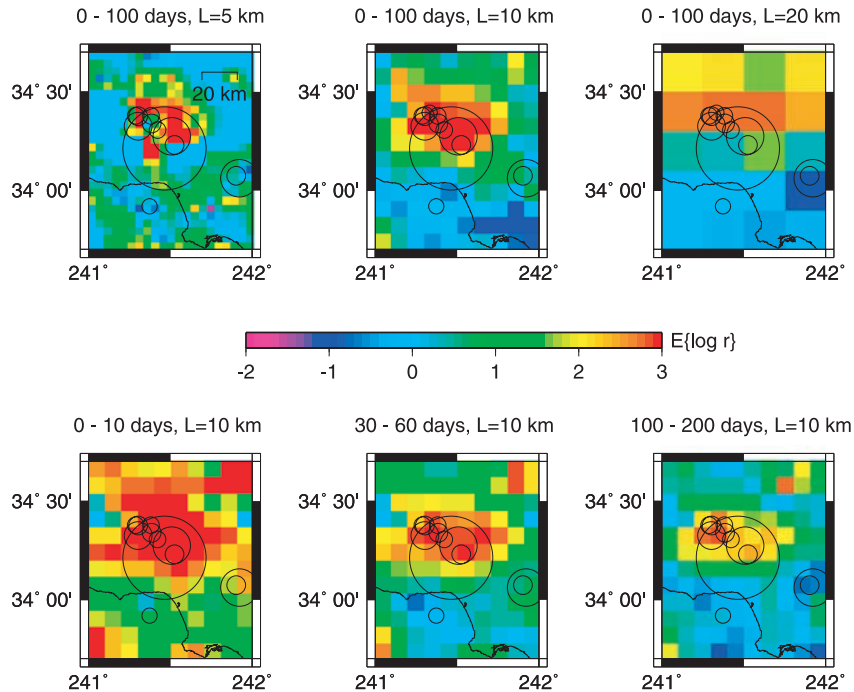


Figure 4. Unbiased seismicity rate change estimator $E\{\log \hat{r}\}$ for the Northridge earthquake (top) for the time interval 0–100 days following the main shock (with a varying discretization length $L = 5, 10$ and 20 km, from left to right) and (bottom) for 0–10 days, 30–60 days and 100–200 days, all with $L = 10$ km. $M5+$ earthquakes that occurred between year 1983 and 200 days after Northridge are shown with circles (radii arbitrarily increasing with M).

compared, as detailed in section 2, to the predicted seismicity rate. Several time intervals for t_A were analyzed, in order to study how the triggering evolves with time. The following parameters were considered:

[36] 1. The magnitude threshold M_c was fixed to 2.3, 1.9 and 1.0 for the Landers, Northridge (SCSN catalogue) and Loma Prieta (NCSN catalogue) data sets, respectively. This threshold was made according to a magnitude-frequency analysis for the selected areas, as documented in Appendix B.

[37] 2. The inversion was performed using a Levenberg-Marquardt algorithm, the model consisting of a linear combination of P power laws. P is dependent on the total number of earthquakes occurring in the cell before T_0 . The inversion was done in two steps: (1) all the parameters were first inverted and (2) a second inversion was then performed after keeping the starting times τ_i constant. This method significantly improved the selection of the scaling factors A_i and the exponents p_i , compared to a one-step inversion. The seismicity in cells that experience significant bursts of preactivity just prior to the main shock are generally badly modeled with this method. For such cells, the discretized ETAS model was used instead.

[38] 3. Cells with too few earthquakes, and cells for which the inversion error is found to be too large, were given a triggering probability $\mathcal{P} = 0.5$ and a mean log ratio $E\{\log \hat{r}\} = 0$. Such a choice is justified by the fact that, if too little is known of the seismogenic process of the cell

(i.e., not enough data), then no decision can be made in favor of either triggering or inhibition, hence a neutral value representing a neutral belief is taken.

3.1. Northridge

[39] The changes in seismicity following the 1994 Northridge earthquake are shown in Figure 4, at various time intervals and for different discretizing lengths L . No significant alteration of the image is obtained by changing L (Figure 4, top), for the 0–100 day interval after Northridge: clear triggering is observed at and around the epicenter, within the rupture zone, and some limited zones of quiescence are seen to emerge from a background of low positive changes at $L = 5$ km. The quiescence zone becomes however dominant in the southernmost third of the studied area, at $L = 10$ km and 20 km. This dependence on L can be removed by considering full space-time seismicity models, in place of the present, purely temporal models that treat each cell separately from the others.

[40] Dependence of the seismicity changes on the time interval under study is very significant, as shown in Figure 4 (bottom). Intense triggering is seen at 0–10 days, over most of the region, while quiescence appears south of the epicenter after 1 month following the main shock, to become dominant between 100 and 200 days. This change in pattern is not due to a less “unfair” estimator that would be incapable of measuring negative changes at short timescales, since the present estimator has been defined to yield unbiased estimates. The emergence

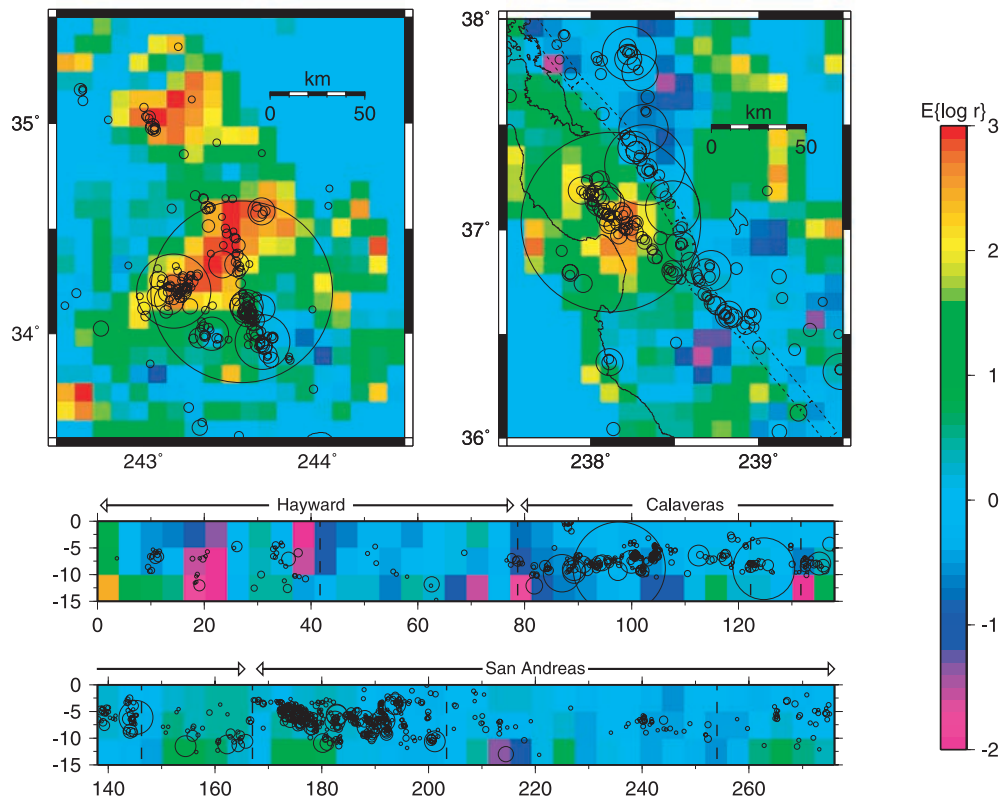


Figure 5. Unbiased seismicity rate change estimator $E\{\log \hat{r}\}_3$, (top left) for the Landers and (top right) the Loma Prieta earthquakes, for 0–100 days after the main shocks, and $L = 10$ km. (bottom) A section with $L = 5$ km along the Hayward, Calaveras, and San Andreas faults. The area probed in this section is shown in dashed lines on the map (Figure 5, top right). Earthquakes of magnitude $M4+$ and $M3+$ are shown, for Figures 5 (top) and 5 (bottom), respectively, with radii arbitrarily increasing with magnitude.

at longer timescales of quiescence, from positively triggered (at short timescales) regions, can be explained by either the existence of two distinct triggering mechanisms, or by a fundamental change in the seismic response of the crust with time. The two explanations are discussed in section 5.

3.2. Landers

[41] Seismicity rate changes for Landers were estimated by *Wyss and Wiemer* [2000], *Kilb et al.* [2000], and *Gomberg et al.* [2001], at rather long timescales (12.5 years before versus 7 years after, and about 8 years before versus 9 months after Landers, for the first two studies, respectively), except for *Gomberg et al.* [2001], who examined the first 2 weeks after Landers. *Wyss and Wiemer* [2000] and *Kilb et al.* [2000] declustered the catalogue, but very different results were obtained: two large lobes of quiescence were seen (one east of Landers, south of the forthcoming Hector Mine earthquake, and one northwest of Big Bear [cf. *Wyss and Wiemer*, 2000, Figure 2]) by *Wyss and Wiemer* [2000], while *Kilb et al.* [2000] report negative changes restricted to a small set of places (mostly south and southwest of Landers, [cf. *Kilb et al.*, 2000, Figure 2]). Such a departure between the two analyses might be due to the difference in the length of the time interval used to estimate the triggering after the

main shock (9 months compared to 7 years), and probably also to a lack of robustness in the declustering procedure. *Gomberg et al.* [2001] only show positive values of the β statistics, but this comes from the choice of the color range made by the authors as negative values were not considered as being reliable, for such a short time interval of between zero and two weeks following the main shock (*J. Gomberg*, personal communication, 2003).

[42] The present method was applied to this sequence, using $L = 10$ km and for the 0–100 day interval immediately following the Landers earthquake (Figure 5, top left). Triggering is observed in most places, with the exception of some quiescence east of the Joshua Tree rupture zone/south of the future site of the Hector Mine earthquake, and along parts of the San Andreas fault. Compared to prediction based on Coulomb stress modeling [*Jaumé and Sykes*, 1992; *King et al.*, 1994], quiescence is relatively lacking. Along the San Andreas, stress calculations by *Jaumé and Sykes* [1992] show small, negative Coulomb stress changes north of the projection of the Big Bear epicenter (at about 34° and 243°), which correlates relatively well with the present observations with mixed positive and negative seismicity changes in this region. The San Gorgonio Pass region, as defined by *Jaumé and Sykes* [1992], is found to experience positive (northernmost half) and negative (south-

ernmost half) seismicity changes, which correlate well to Coulomb stress calculations on strike-slip, vertical faults, but not to a set of reverse slip faults as proposed by *Jaumé and Sykes* [1992]. Coulomb stress changes, on optimally oriented strike-slip, vertical faults, have been computed following the Landers and the Big Bear earthquakes by *King et al.* [1994]. Comparison with the seismicity rate changes of Figure 5 shows the absence of quiescence east and north of the Landers rupture, contrary to what would be predicted by *King et al.* [1994]. While the few cells found with negative seismicity changes correlate well with stress shadows, too few of them are obtained, overall. The present estimates of seismicity changes relate to both Landers and Big Bear, while Joshua Tree is not considered as a trigger (its aftershock sequence is accounted for by the nonstationary seismicity model of section 2). As a result, the quiescence observed east of Joshua Tree is due to stress changes caused by Landers.

3.3. Loma Prieta

[43] Seismicity changes following the Loma Prieta earthquake have been analyzed by *Reasenber and Simpson* [1992, 1997], *Simpson and Reasenber* [1994], and *Parsons et al.* [1999] [see also *Stein*, 1999]. Surface creep changes have also been detected and compared to stress changes [*Lienkaemper et al.*, 1997]. These studies agree that (1) there seems to exist a significant correlation between stress changes and seismicity or surface creep changes; (2) mainly positive triggering is observed, especially on the rupturing segment of the San Andreas; (3) the results are ambiguous for the Calaveras fault, where the 1984 $M6.1$ Morgan Hill earthquake strongly disturbed the seismicity up to the time of the Loma Prieta earthquake, and (4) a clear instance of quiescence is found for the southernmost, creeping segment of the Hayward fault (at about 37.45° and -121.8°), a segment that previously experienced the neighboring influence of the Morgan Hill earthquake.

[44] The unbiased seismicity rate change $E\{\log \hat{r}\}$ at $0 < t_A < 100$ days is shown in Figure 5 (top right and bottom). Figure 5 (bottom) corresponds to a section roughly following segments of the Hayward, Calaveras, and San Andreas faults. As documented in the previous studies cited above, inhibition of the seismicity is mainly observed along and east of the Hayward fault, including both its southernmost segment studied by *Lienkaemper et al.* [1997] and the area where the Mount Lewis earthquake occurred. The Calaveras and the San Gregorio faults are seen to globally undergo positive triggering, even though, in the case of the Calaveras fault, the section along depth (Figure 5, bottom) reveals quiescent patches. Modeling of the static stress generated by the Loma Prieta earthquake shows that the south Hayward fault experienced a reduction in right-lateral shear stress $\Delta\tau \simeq -2$ bars along with an increase in normal stress, i.e., unclamping $\Delta\sigma_n \simeq +3$ bars [*Parsons et al.*, 1999] or, equivalently, a decrease in Coulomb stress $\Delta\sigma \simeq -2$ bars, for a (low) friction coefficient $\mu = 0.2$ [*Reasenber and Simpson*, 1992]. The latter study also reports a positive change of Coulomb stress, albeit small ($\Delta\sigma \simeq 0 - 1$ bar) for most of the Calaveras fault, south of the Morgan Hill epicenter. The northern segment of the Hayward fault was found to be slightly relaxed (with $|\Delta\text{CFF}| < 0.4$ bar), while the San Gregorio fault alternates positive and negative

Coulomb stresses. The seismicity rate changes calculated here show good correlation with this modeling for the Hayward fault, but not so for the San Gregorio nor the Calaveras faults. Inspection of the time series indeed show very little changes in the activity on the latter fault, south of the Morgan Hill epicenter.

[45] The quiescence observed near the southern end of the Hayward and north Calaveras faults corresponds to a zone characterized by a strongly spatially variable, low p exponent for the modified Omori's law, as already noticed by *Schaff et al.* [1998] for Morgan Hill aftershocks on the Calaveras, and by *Wiemer and Katsumata* [1999]. This p exponent is computed on Figure 6 for relocated (using cross-spectral analysis leading to estimates of the relative locations between events) aftershocks of the Morgan Hill earthquake, using a simple least squares estimator and a t^{-p} model for the seismicity time series for $t > 0$ following Morgan Hill. A clear transition at about 3–4 km north of the Morgan Hill hypocenter is seen, separating low p values ($p < 0.3$) to the north, from more usual p values with a $p \simeq 0.6$ average, to the south. This transition is coincidental with the transition between a clear decrease of seismicity to the north (hence for low p values) and little seismicity change to the south (higher p values). Lateral variations in frictional properties can explain part of the observed seismicity change distribution around the Morgan Hill hypocenter, with clearly marked quiescence corresponding to (globally) velocity strengthening segments.

4. Relative Absence of Shadowing Effects Analyzed by Direct Correlation Measures

[46] The relative absence of quiescence, as compared to typical predictions based on Coulomb modeling of earthquake interactions, can also be seen by direct correlation analysis. When considering the activities of two given crustal volumes, one expects them to behave independently of each other unless a strong enough earthquake causes significant stress changes on both locations; two cases can then be distinguished: either (1) the two volumes are both activated or both inhibited, resulting in positively correlated fluctuations of their activities or (2) one place is inhibited while the other is activated, hence a negative correlation between the two volumes. Roughly speaking, case 1 implies that the two zones “do the same thing (either increase or decrease of activity) at the same time”, and case 2 implies that they “do opposite things at the same time”. If on average a portion p of the total crustal volume experiences positive triggering, hence $1 - p$ experiences quiescence, then case 1 is found with probability $p^2 + (1 - p)^2$, while case 2 has probability $2p(1 - p)$. Coulomb modeling predicts probabilities p close to 0.5 (or slightly higher, if considering that the causative fault is characterized by positive Coulomb stresses), hence inhibition and positive triggering, therefore positive and negative correlations between two arbitrary crustal volumes, should be observed with roughly equal probabilities.

[47] Linear correlation coefficients ρ are computed for southern and central California earthquakes (6824 $M3+$ earthquakes occurring between 1981 and 1999, with latitude ranging between 32° and 37° , longitude between -121° and -115°), after discretizing the area in cells of

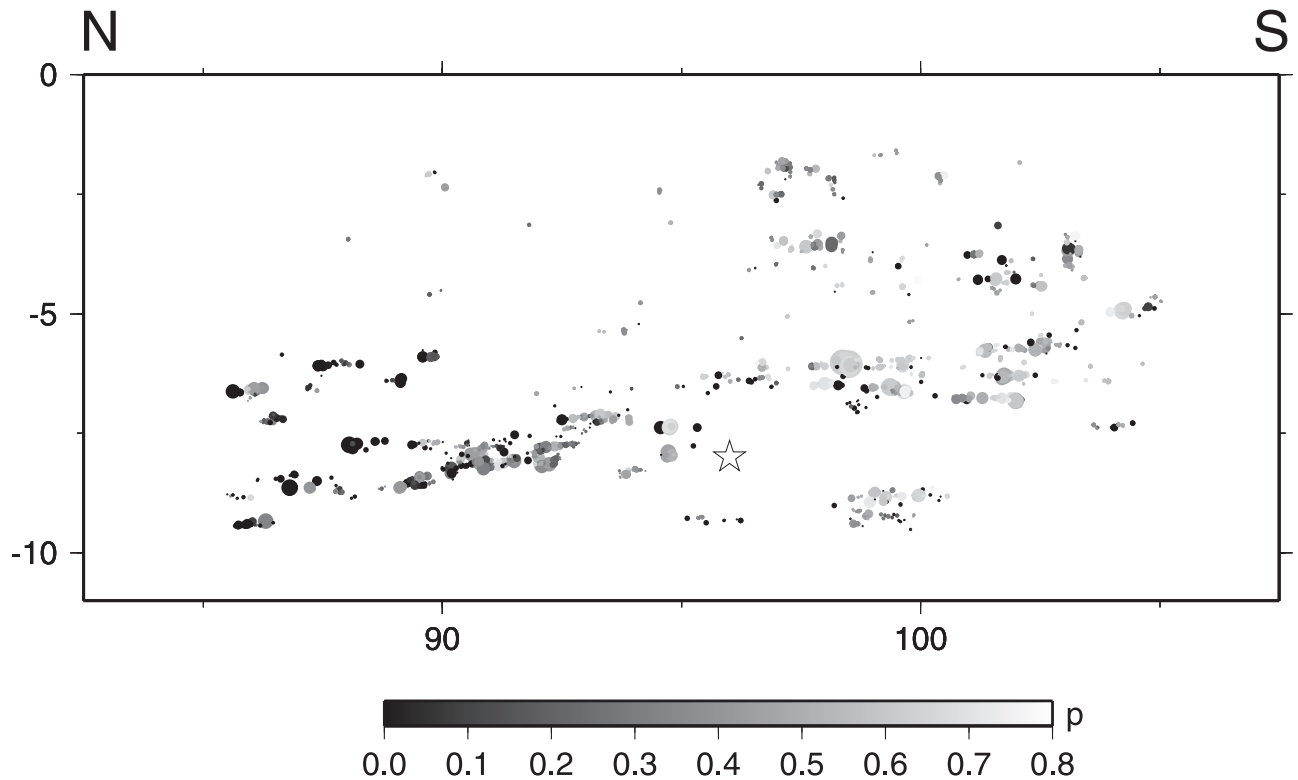


Figure 6. Estimate of the p exponent for the modified Omori's law, for a segment of the Calaveras fault (Figure 5) using relocated earthquakes. The horizontal coordinate (in km) is the same as in Figure 5, depth (vertical axis) is also in km. The hypocenter of the Morgan Hill earthquake is shown with a star. A rather sharp transition is observed between low (in the north) and higher (in the south) p values that correlates well with the change in response following the Loma Prieta earthquake shown in Figure 5 (quiescence for low p , positive triggering for large p).

$10 \times 10 \text{ km}^2$. For every pair of (distinct) cells with intercell distance less than 100 km, the linear correlation coefficient $\rho_{ij} = \{\text{Cov}[s_i(t), s_j(t + \Delta t)]\} / \{\sigma_i \sigma_j\}$ is computed, where $\text{Cov}[s_1(t), s_2(t + \Delta t)]$ is the covariance of the two activity time series in cell i and cell j , with time separation of Δt , and σ_i and σ_j are their standard deviations. Probability distributions of the coefficients ρ_{ij} are thus obtained, and compared in Figure 7 to equivalent distributions that would have been obtained by pure chance. The latter null hypothesis corresponds to uniformly drawing the occurrence times of the earthquakes without changing the location of their epicenters. The correlation coefficients are then distributed according to a law derived in Appendix C.

[48] Four cases are studied: (1) discretization in time using 10-day bins, and $\Delta t = 0$, (2) discretization in time using 10-day bins, and $\Delta t = 90$ days, (3) discretization in time using 100-day bins, and $\Delta t = 0$, and (4) discretization in time using 100-day bins, and $\Delta t = 900$ days. In all four cases, positive correlation $\rho > 0$ is observed to be significantly (well above the 95% confidence interval) more frequent than for the null hypothesis, while negative correlation $\rho < 0$ is too rarely obtained compared to the null hypothesis. It is also noted that ρ is biased toward positive values, since the null hypothesis yields $\rho > 0$ much more frequently than $\rho < 0$. The latter case is however clearly more frequent for the null hypothesis than in the real data. This confirms the observation that quiescence is rather insignificant, for the timescales studied (up to 1000 days).

Similar results are obtained when changing the maximum distance (here equal to 100 km) between cells for which the correlation coefficient is computed: any two cells tend to be uncorrelated as the distance increases between them, and therefore increasing this maximum intercell distance only results in increasing the relative proportion of low valued ρ s.

5. Discussion

[49] The question remains as to why a region, or more exactly a fault, that is on average unloaded (decrease of static Coulomb stress), can still experience an increase of seismicity, at least at the short timescales studied in this paper. Triggering by dynamic stresses [Hill *et al.*, 1993; Gombert, 1996] is a natural candidate; the areas examined in the present paper are about twice the length of the main shock rupture, and thus experience dynamic stresses that are not on average significantly greater than the static component. Predictive models or observations of how the intensity of triggering vary with the amplitude of the waves, their frequency content, and the remanent static stress, need to be considered in order to examine whether an initial period characterized by triggering can eventually make way to quiescence.

[50] Global stress decrease, along with increase of seismicity, is characteristic of the causative fault: shear stress is on average reduced by the occurrence of the main shock, but large numbers of aftershocks are triggered on the fault. Heterogeneity of the stress change, due to a variable (at

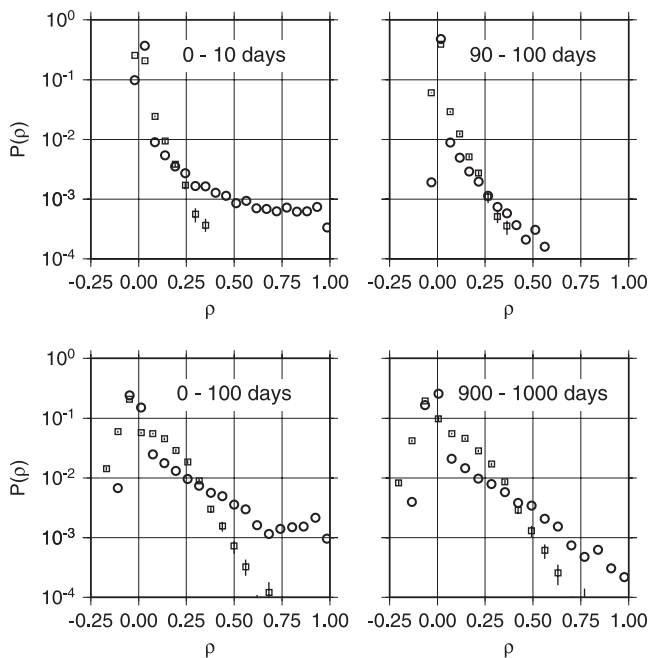


Figure 7. Distribution of the linear correlation coefficient ρ for southern and central California discretized in $10 \times 10 \text{ km}^2$ cells. Circles indicate actual values, and squares indicate distribution for the null hypothesis (earthquake occurrence times uniformly randomized), along with an estimate of the 95% interval (error bars). Four cases are considered, by changing the length of the time bins over which the time series are discretized (10 day bins for the top graphs, 100 day bins for the bottom graphs) and the separation in time (time lag) Δt between the two series ((left) $\Delta t = 0$ and (right) $\Delta t = 90$ days and $\Delta t = 900$ days, from top to bottom). Positive correlation is significantly more frequent in the real case compared to the null hypothesis, while there is a strong deficit of negative correlation for the former. The correlation decays when considering nonzero time lags Δt , as expected for any decorrelating process: in the limit $\Delta t \rightarrow \infty$ the actual distribution converges toward the one of the null hypothesis.

small scale) slip distribution, can explain this common observation [e.g., *Bouchon, 1997*]. Also, loading (or unloading) of a rock volume or sample containing complex sets of fractures generates complex, strongly heterogeneous stress changes. Geodetic measurements, for example by radar interferometry, of the displacements following an earthquake, can only image the very large scale feature of this heterogeneity in stress, as they integrate over, hence smooth it (an example is given by *Fialko et al. [2002]*, in the case of the Hector Mine earthquake). It can be expected that the stress changes undergone by the crust following an earthquake are therefore much more fluctuating than the changes computed by dislocation models in homogeneous (or even layered) elastic half-spaces. Horizontal stress orientations measured down a borehole at Cajon Pass, 4 km off the San Andreas fault, have been shown to fluctuate in a scale-invariant way with depth [*Shamir and Zoback, 1992*]. Such fluctuations have been interpreted as resulting from numerous superpositions of stress perturbations caused by the local faults and fractures crossed by the

borehole. More generally, estimates of the elastic parameters from sonic velocities measurements in various boreholes have also been observed to exhibit large, scale-invariant fluctuations, that could result from complex fracture sets and self-similar lithological distribution [*Leary, 1991; Wu et al., 1994; Holliger, 1996; Bean, 1996; Marsan and Bean, 1999*]. The ubiquity of the latter observations is remarkable. Stress changes caused by a major earthquake can thus be expected to be significantly variable in space, and to be controlled at first order by both the complex slip distribution (close to the fault) and the heterogeneity of the elastic medium (close to and further away from the fault). Any given crustal volume subject to an average stress decrease (on optimally oriented faults, for instance), will contain subvolumes characterized by stress increases. Nonsymmetric response, in terms of earthquake occurrence rates, of a fault to positive or negative Coulomb stress changes, combined with such a strongly fluctuating stress perturbation, can explain the present observation of the relative oddity of quiescence zones. Rate-and-state friction exhibits such a nonsymmetric response; seismicity rate changes are expected to be proportional, at short timescales, to $\exp(\Delta\tau/A\sigma)$, where $\Delta\tau$ is the change in shear stress, σ the normal stress acting on the target fault, and A a constitutive parameter [*Dieterich, 1994*]. In this model, regions experiencing an average large, negative, but strongly fluctuating (due to the heterogeneity of the medium) change in shear stress, can yield an average increase of activity rather than quiescence. The latter would only develop with time, as the asymmetry of the response is reduced.

6. Conclusions

[51] The main results of the present analyses are as follows:

[52] 1. Poisson statistics can be developed in order to account for both the nonstationarity of earthquake population dynamics and the bias in favor of triggering.

[53] 2. Changes in seismicity related to the occurrence of a large earthquake are strongly time-dependent, and therefore comparison with static, i.e., constant, stresses is ambiguous.

[54] 3. Positive triggering is significantly more frequently observed than quiescence, the more so as the time interval after the main shock is reduced.

[55] 4. Several instances of significant misfit between the calculated seismicity rate changes and the modeled static Coulomb stress changes are found. This shows that the large-scale, static Coulomb stress does not systematically control the seismicity occurring within the first few months following an earthquake.

[56] 5. Heterogeneity of the medium, combined with a nonsymmetric response of the crust to positive/negative changes in shear stress, can possibly explain these observations, as would the existence of a distinct triggering regime, at short timescales, due to the dynamic transient in stress caused by the passage of the seismic waves.

Appendix A: Unbiasing $E\{\log \hat{r}\}$

[57] The biased $E\{\log \hat{r}\}$ as defined in section 2.4 can be studied for the stationary model of section 2.2. Knowing λ_A and λ_B , and given t_A and t_B , the probability density

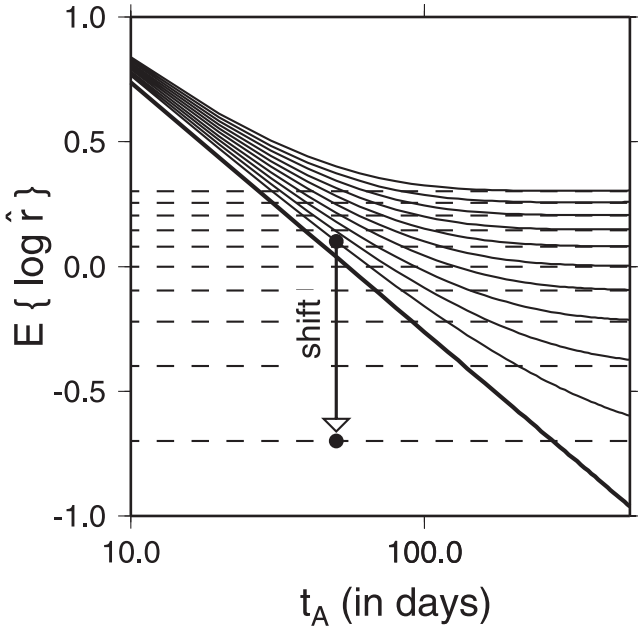


Figure A1. $E\{\log \hat{r} | \lambda_A, \lambda_B\}$ for $\lambda_B = 0.01$ earthquake per day, $t_B = 100$ days, and $\lambda_A = 0.002, 0.004, 0.006, \dots, 0.02$ earthquake per day (from bottom to top), in the stationary case. The limit $\lambda_A \rightarrow 0$, as given by equation (A3), is shown by the thick line. Expected log ratios $\log \lambda_A/\lambda_B$ are shown by dashed lines. A minimum timescale t_A is needed for $E\{\log \hat{r}\}$ to approximate $\log \lambda_A/\lambda_B$, the smaller λ_A the longer. In order to unbiased the estimator $E\{\log \hat{r}\}$, a negative shift is required (e.g., arrow, in the case $\lambda_A = 0.002$ earthquake per day and $t_A = 50$ days).

functions $f_A(\hat{\lambda}_A | \lambda_A)$ and $f_B(\hat{\lambda}_B | \lambda_B)$ can be calculated, since $f(\hat{\lambda} | \lambda) = \sum_{n=0}^{\infty} P(n | \lambda t) P(\hat{\lambda} | n)$. This simply gives that

$$f(\hat{\lambda} | \lambda) = t e^{-(\lambda + \hat{\lambda})t} \sum_{n=0}^{\infty} \frac{(\lambda \hat{\lambda} t^2)^n}{(n!)^2} \quad (\text{A1})$$

This is then used in order to estimate

$$E\{\log \hat{r} | \lambda_A, \lambda_B\} = \int_0^{\infty} d\hat{\lambda} \log \hat{\lambda} \{f_A(\hat{\lambda} | \lambda_A) - f_B(\hat{\lambda} | \lambda_B)\} \quad (\text{A2})$$

In the limit $\lambda_A t_A \rightarrow 0$, i.e., in the case of regions becoming very weakly active and short timescales t_A , $f_A(\hat{\lambda}_A | \lambda_A) \simeq t_A \exp(-\hat{\lambda}_A t_A)$, and the estimator converges toward

$$\lim_{\lambda_A t_A \rightarrow 0} E\{\log \hat{r} | \lambda_A, \lambda_B\} = -\gamma - \log t_A - E\{\log \hat{\lambda}_B | \lambda_B\} \quad (\text{A3})$$

where $\gamma \simeq 0.557$ is Euler's constant. In this limit, $E\{\log \hat{r} | \lambda_A, \lambda_B\}$ is independent of λ_A , implying that it cannot correctly measure seismicity rate changes for such regions and timescales. Note that a similar treatment leads to $\lim_{\lambda_A t_A \rightarrow 0} \mathcal{P} = E\{-e^{\lambda_B t_A} | \lambda_B\}$. Figure A1 shows an example of how $E\{\log \hat{r}\}$ decays to $\log \lambda_A/\lambda_B$ as t_A is increased, for $\lambda_B = 10^{-2}$ earth-

quake/day, $t_B = 100$ days, and λ_A varying between 2×10^{-3} and 2×10^{-2} earthquake per day. $E\{\log \hat{r}\}$ gives a good estimate of the expected $\log \lambda_A/\lambda_B$ when t_A is large enough. For too small a t_A , a significant departure from $\log \lambda_A/\lambda_B$ is seen, possibly resulting in the observation of an artificial positive triggering. For example, $\lambda_A = 0.006$ earthquake/day would correspond to an actual quiescence, since the seismicity rate λ_A is 1.67 times lower than the preseismicity rate λ_B ; however, an observation made at $t_A = 10$ days would give $E\{\log \hat{r}\} = 0.78$, i.e., an apparent positive triggering. Only for t_A greater than about 500 days would $E\{\log \hat{r}\}$ be relatively close to the expected $\log \lambda_A/\lambda_B = -0.22$.

[58] $E\{\log \hat{r}\}$ and \mathcal{P} are therefore biased, for too small a t_A . \mathcal{P} is unbiased when $t_A = t_B$, i.e., it yields $\mathcal{P} > 0.5$ when $\lambda_A > \lambda_B$ and $\mathcal{P} < 0.5$ when $\lambda_A < \lambda_B$. The bias on $E\{\log \hat{r}\}$ vanishes for large t_A . A correction to this estimator can be given in order to unbiased it. Practically, in the nonstationary case (i.e., the one that needs to be considered for real data), the maximum likelihood estimate $\hat{\lambda}_B^*$, hence the one maximizing $f_B(\hat{\lambda}_B)$, is used as our "best guess" on λ_B . Then, knowing λ_B, t_B and t_A , λ_A is searched such that $E\{\log \hat{r} | \lambda_A, \hat{\lambda}_B^*\}$ of the stationary model equals the estimated $E\{\log \hat{r}\}$ of section 2.4. The log ratio $\log \lambda_A/\hat{\lambda}_B^*$ is then taken as the new estimator. This operation corresponds to shifting $E\{\log \hat{r}\}$, as shown in Figure A1, to the expected log ratio.

Appendix B: Completeness of Data

[59] In order to estimate the minimum magnitude of completeness of the three data sets analyzed in this manuscript, the following procedure is taken:

[60] 1. The b value and the log likelihood of completeness are computed for all earthquakes with magnitude greater than m . The b value is computed using the discrete Gutenberg-Richter model of *Utsu* [1966], with magnitude bands of width $\delta m = 0.1$. No uncertainties on the magnitudes were assumed. The log likelihood of completeness is the logarithm of the probability that the best Gutenberg-Richter law fitted against all the earthquakes with magnitudes greater than m can predict the number of earthquakes with magnitude ranging between $m - \delta m$ and m .

[61] 2. The minimum magnitude of completeness M_c is chosen so that (1) the b value drops for $m < M_c$ and (2) the log likelihood drops for $m = M_c$. This indicates that significantly too few earthquakes occur with magnitudes $m < M_c$ as would be expected from the best Gutenberg-Richter law deduced from the magnitudes $\geq M_c$.

[62] Figure B1 shows this procedure, for the first year of aftershock around Landers (33.5° to 35.5° , -117.5° to -115°). The minimum magnitude of completeness is found to be $M_c = 2.3$, as shown by the arrows on Figures B1 (middle) and B1 (bottom). The log likelihood is also observed to drop at $m = 2.9$, but this corresponds to an increase in b , hence a larger number of earthquakes compared to the best Gutenberg-Richter prediction.

[63] The minimum magnitude of completeness is computed independently for the preseismicity and for one year of postseismicity, for the three data sets. The maximum magnitude is then chosen between the post- and the pre- M_c for each data set, to be the overall magnitude of completeness. This yields $M_c = 2.3, 1.9$ and 1.0 for Landers, North-

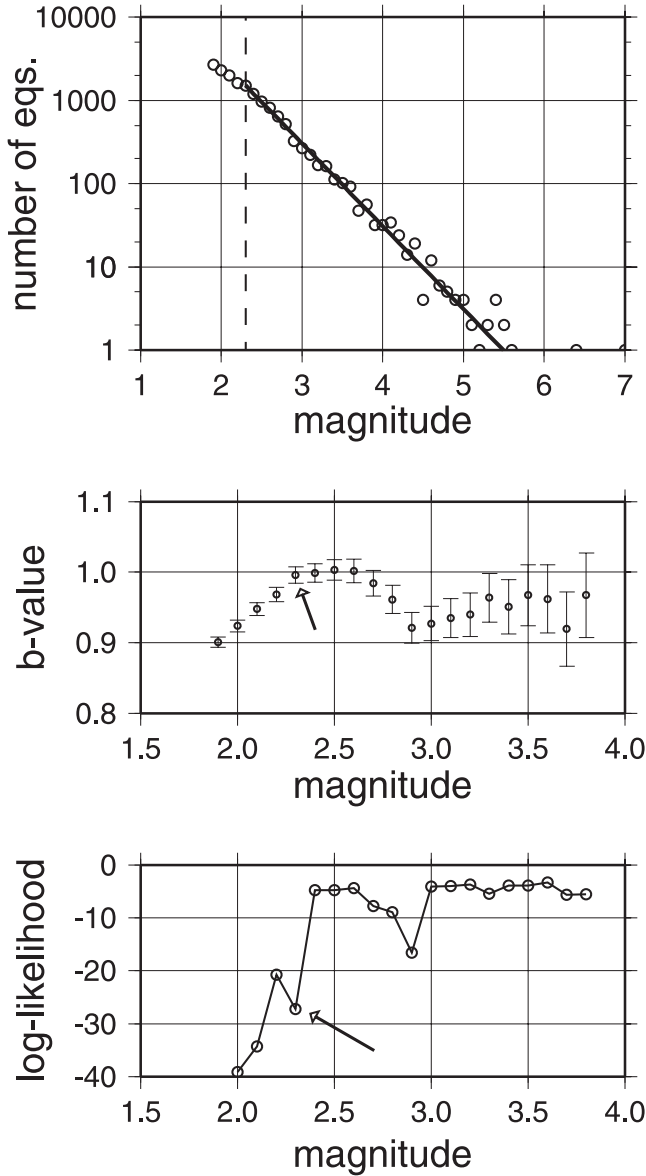


Figure B1. Selection of the minimum magnitude of completeness, in the case of one year of postseismicity in the region of Landers. (top) Magnitude-frequency graph, for magnitude bands of width $\delta m = 0.1$. Completeness is observed for magnitudes greater than or equal to 2.3 (dashed line). The best Gutenberg-Richter law is shown in thick line, corresponding to $b = 0.996 \pm 0.012$. (middle) Variations of the b value, along with its uncertainty, with the cutoff magnitude m (all earthquakes with magnitude $\geq m$ are used to estimate b). b is seen to drop for $m < 2.3$ (arrow). (bottom) Log likelihood of the observed number of earthquakes with magnitude between $m - \delta m$ and m , given the best Gutenberg-Richter model obtained for the earthquakes with magnitudes $\geq m$. The log likelihood drops at $m = 2.3$ (arrow), showing that the number of $m = 2.2$ ($\pm \delta m/2$) earthquakes is significantly overestimated by the Gutenberg-Richter law given by the $M_{2.3+}$ earthquakes.

ridge and Loma Prieta, respectively. Spatial variations in M_c can be observed, e.g., by considering subregions. Such variations are not too strong; a maximum $\Delta M_c = 0.4$ is obtained for Loma Prieta, when looking at $50 \times 50 \text{ km}^2$ regions. Note also that the method described in section 2 is only sensitive to temporal changes in M_c , but very little to spatial changes since all the cells are treated independently from each other.

Appendix C: Distribution of the Linear Correlation Coefficient ρ for Two Independent, Purely Random Time Series

[64] The null hypothesis considered in section 4, to be compared to the real catalogue, is one for which the earthquakes are kept at their actual epicenter locations but are given a random time of occurrence (i.e., their occurrence time is a uniform random variable). The distribution $P(\rho)$ of the correlation coefficient ρ for all pairs of cells is here derived, for this null hypothesis.

[65] Consider two time series $s_1(n)$ and $s_2(n)$, $n = \{1, \dots, N\}$, such that the total numbers of earthquakes are $\mathcal{N}_1 = N\bar{s}_1$ and $\mathcal{N}_2 = N\bar{s}_2$, where \bar{s} is the sample mean. Then

$$\rho = \frac{\sum_{n=1}^N s_1(n)s_2(n) - \mathcal{N}_1\mathcal{N}_2/N}{\sqrt{\sum_{n=1}^N (s_1(n) - \mathcal{N}_1/N)^2 \sum_{n=1}^N (s_2(n) - \mathcal{N}_2/N)^2}} \quad (\text{C1})$$

Assuming, as is very generally observed (as long as the cell size L is small enough), that $\bar{s}_1 \ll 1$ and $\bar{s}_2 \ll 1$, then the time series $\pi(n) = s_1(n)s_2(n)$, $n = \{1, \dots, N\}$, is binary, with $\text{Pr}(\pi = 1) = \mathcal{N}_1\mathcal{N}_2/N^2$ and $\text{Pr}(\pi = 0) = 1 - \mathcal{N}_1\mathcal{N}_2/N^2$. The sum $\Pi = \pi(1) + \dots + \pi(N)$ is therefore a Poisson random variable with mean $\lambda = \mathcal{N}_1\mathcal{N}_2/N$. It is also straightforward to show that the variances of s_1 and s_2 are $\text{var}(s) \simeq \mathcal{N}(1 - \mathcal{N}/N)$. This yields that $P(\rho) = \exp(-\lambda) \lambda^\Pi / \Pi!$, with integer $\Pi = a\rho + b$, $\lambda = \mathcal{N}_1\mathcal{N}_2/N$, $a = \sqrt{\mathcal{N}_1\mathcal{N}_2}/[1 + (\mathcal{N}_1 + \mathcal{N}_2)/2N]$ and $b = \sqrt{\mathcal{N}_1\mathcal{N}_2}/N$. The distribution of ρ for the null hypothesis is obtained from these relations, with $(\mathcal{N}_1, \mathcal{N}_2)$ taking all possible observed pairs, for the grid used in the analysis.

[66] **Acknowledgments.** I would like to acknowledge financial support from the EC funded PRESAP research project, from the CNRS “ACI Prévention des Catastrophes Naturelles”, and from the LGIT research group on “Fluids and dynamics of the crust”. I also would like to thank J. L. Got, J. McCloskey, S. Steacy, D. Baumont, O. Scotti, M. Cocco, C. Bean, and my colleagues from the “Fluids and dynamics of the crust” research group for helpful discussions and advices, and B. Valette for his help with some of the mathematical developments of section 2.4. Remarks, critics and suggestions by Ruth Harris, an anonymous reviewer and the associate editor, considerably helped improving the quality of this manuscript. The seismicity data sets were provided by the Northern California Earthquake Data Center (NCSN catalogue), the Southern California Earthquake Center (SCSN catalogue), the member networks of the Council of the National Seismic Systems (CNSS catalogue), and Allan Rubin and Alon Ziv for the relocated Calaveras seismicity data set.

References

- Bean, C. J., On the cause of 1/f-power spectral scaling in borehole sonic logs, *Geophys. Res. Lett.*, 23, 3119–3122, 1996.
 Bouchon, M., The state of stress on some faults of the San Andreas system as inferred from near-field strong motion data, *J. Geophys. Res.*, 102, 11,731–11,744, 1997.

- Dieterich, J. H., A constitutive law for rate of earthquake production and its application to earthquake clustering, *J. Geophys. Res.*, *99*, 2601–2618, 1994.
- Dieterich, J. H., and P. G. Okubo, An unusual pattern of recurring seismic quiescence at Kalapana, Hawaii, *Geophys. Res. Lett.*, *23*, 447–450, 1996.
- Ellsworth, W. L., A. G. Lindh, W. H. Prescott, and D. G. Herd, The 1906 San Francisco earthquake and the seismic cycle, in *Earthquake Prediction: An International Review*, Maurice Ewing Ser., vol. 4, edited by D. W. Simpson and P. G. Richards, AGU, Washington, D. C., 1981.
- Felzer, K. R., T. W. Becker, R. E. Abercrombie, G. Ekström, and J. R. Rice, Triggering of the 1999 M_w 7.1 Hector Mine earthquake by aftershocks of the 1992 M_w 7.3 Landers earthquake, *J. Geophys. Res.*, *107*(B9), 2190, doi:10.1029/2001JB000911, 2003.
- Fialko, Y., D. Sandwell, D. Agnew, M. Simons, P. Shearer, and B. Minster, Deformation on nearby faults induced by the 1999 Hector Mine earthquake, *Science*, *297*, 1858–1862, 2002.
- Gomberg, J., Stress/strain changes and triggered seismicity following the M_s 7.4 Landers, California, earthquake, *J. Geophys. Res.*, *101*, 751–764, 1996.
- Gomberg, J., P. A. Reasenberg, P. Bodin, and R. A. Harris, Earthquake triggering by seismic waves following the Landers and Hector Mine earthquakes, *Nature*, *411*, 462–466, 2001.
- Harris, R. A., Introduction to special section: Stress triggers, stress shadows, and implications for seismic hazard, *J. Geophys. Res.*, *103*, 24,347–24,358, 1998.
- Harris, R. A., and R. W. Simpson, In the shadow of 1857—Effect of the great Ft. Tejon earthquake on subsequent earthquakes in southern California, *Geophys. Res. Lett.*, *23*, 229–232, 1996.
- Harris, R. A., and R. W. Simpson, Suppression of large earthquakes by stress shadows: A comparison of Coulomb and rate-and-state failure, *J. Geophys. Res.*, *103*, 24,439–24,451, 1998.
- Hill, D. P., et al., Remote seismicity triggered by the $M7.5$ Landers, California earthquake of June 28, 1992, *Science*, *260*, 1617–1623, 1993.
- Holliger, K., Fault scaling and 1/f noise scaling of seismic velocity fluctuations in the upper crystalline crust, *Geology*, *24*, 1103–1106, 1996.
- Jaumé, S. C., and L. R. Sykes, Changes in state of stress on the southern San Andreas fault resulting from the California earthquake sequence of April to June 1992, *Science*, *258*, 1325–1328, 1992.
- Jaumé, S. C., and L. R. Sykes, Evolution of moderate seismicity in the San Francisco Bay region, 1850 to 1993: Seismicity changes related to the occurrence of large and great earthquakes, *J. Geophys. Res.*, *101*, 765–789, 1996.
- Kagan, Y. Y., and D. D. Jackson, Long-term earthquake clustering, *Geophys. J. Int.*, *104*, 107–133, 1991.
- Kilb, D., J. Gomberg, and P. Bodin, Triggering of earthquake aftershocks by dynamic stresses, *Nature*, *408*, 570–574, 2000.
- King, G. C. P., R. S. Stein, and J. Lin, Static stress changes and the triggering of earthquakes, *Bull. Seismol. Soc. Am.*, *84*, 935–953, 1994.
- Leary, P., Deep borehole log evidence for fractal distribution of fractures in crystalline rock, *Geophys. J. Int.*, *107*, 615–627, 1991.
- Lienkaemper, J. J., J. S. Galehouse, and R. W. Simpson, Creep response of the Hayward fault to stress changes caused by the Loma Prieta earthquake, *Science*, *276*, 2014–2016, 1997.
- Marsan, D., and C. J. Bean, Multiscaling nature of sonic velocities and lithology in the upper crystalline crust: Evidence from the KTB main borehole, *Geophys. Res. Lett.*, *26*, 275–278, 1999.
- Ogata, Y., Statistical models for earthquake occurrences and residual analysis for point processes, *J. Am. Stat. Assoc.*, *83*, 9–27, 1988.
- Ogata, Y., Seismicity analysis through point-process modeling: A review, *Pure Appl. Geophys.*, *155*, 471–507, 1999.
- Parsons, T., R. S. Stein, R. W. Simpson, and P. A. Reasenberg, Stress sensitivity of fault seismicity: A comparison between limited-offset oblique and major strike-slip faults, *J. Geophys. Res.*, *104*, 20,183–20,202, 1999.
- Reasenberg, P. A., Second-order moment of central California seismicity, 1969–1982, *J. Geophys. Res.*, *90*, 5479–5495, 1985.
- Reasenberg, P. A., and L. M. Jones, Earthquake hazard after a mainshock in California, *Science*, *243*, 1173–1176, 1989.
- Reasenberg, P. A., and R. W. Simpson, Response of regional seismicity to the static stress change produced by the Loma Prieta earthquake, *Science*, *255*, 1687–1690, 1992.
- Reasenberg, P. A., and R. W. Simpson, Response of regional seismicity to the static stress change produced by the Loma Prieta earthquake, *U.S. Geol. Surv. Prof. Pap.*, *1550-D*, 49–71, 1997.
- Schaff, D. P., G. C. Beroza, and B. E. Shaw, Postseismic response of repeating aftershocks, *Geophys. Res. Lett.*, *25*, 4549–4552, 1998.
- Scientists of the U.S. Geological Survey and the Southern California Earthquake Center, The magnitude 6.7 Northridge, California, earthquake of 17 January 1994, *Science*, *266*, 389–397, 1994.
- Shamir, G., and M. D. Zoback, Stress orientation profile to 3.5 km depth near the San Andreas fault at Cajon Pass, California, *J. Geophys. Res.*, *97*, 5059–5080, 1992.
- Simpson, R. W., and P. A. Reasenberg, Earthquake-induced static stress changes on central California faults, *U.S. Geol. Surv. Prof. Pap.*, *1550-F*, 55–89, 1994.
- Stein, R. S., The role of stress transfer in earthquake occurrence, *Nature*, *402*, 605–609, 1999.
- Toda, S., R. S. Stein, P. A. Reasenberg, J. H. Dieterich, and A. Yoshida, Stress transferred by the 1995 $M_w = 6.9$ Kobe, Japan, shock: Effect on aftershocks and future earthquake probabilities, *J. Geophys. Res.*, *103*, 24,543–24,565, 1998.
- Utsu, T., A statistical significance test of the difference in b-value between two earthquake groups, *J. Phys. Earth*, *14*, 37–40, 1966.
- Wiemer, S., Introducing probabilistic aftershock hazard mapping, *Geophys. Res. Lett.*, *27*, 3405–3408, 2000.
- Wiemer, S., and K. Katsumata, Spatial variability of seismicity parameters in aftershock zones, *J. Geophys. Res.*, *104*, 13,135–13,151, 1999.
- Wu, R. S., Z. Xu, and X. P. Li, Heterogeneity spectrum and scale anisotropy in the upper crust revealed by the German Continental Deep-Drilling (KTB) Holes, *Geophys. Res. Lett.*, *10*, 911–914, 1994.
- Wyss, M., and S. Wiemer, Change in the probability for earthquakes in southern California due to the Landers magnitude 7.3 earthquake, *Science*, *290*, 1334–1338, 2000.
- Zhuang, J., Y. Ogata, and D. Vere-Jones, Stochastic declustering of space-time earthquake occurrences, *J. Am. Stat. Assoc.*, *97*, 369–380, 2002.

D. Marsan, Laboratoire de Géophysique Interne et Tectonophysique, Université de Savoie, Campus Scientifique, F-73376, Le Bourget du Lac cedex, France. (david.marsan@univ-savoie.fr)